Laboratory validation of geoelectrical models for permeability prediction

Andreas Weller[1,*], *Klaudio* Peshtani[2], *Mohamed* Kassab[3], and *Lee* Slater[2]

[1]Clausthal University of Technology, Department of Geosciences, 38678 Clausthal-Zellerfeld, Germany
[2]Department of Earth and Environmental Sciences, Rutgers University, Newark, NJ, USA
[3]Egyptian Petroleum Research Institute, Cairo 11727, Egypt

Abstract. Permeability prediction from non-invasive geophysical measurements or well logging remains a challenge. Different models have been proposed to relate geophysical parameters to permeability. We evaluate the potential of geoelectrical models for permeability prediction using a database composed of 282 samples of sandstone, carbonate, and mudstone formations. The capillary bundle model (CBM) describes permeability k in terms of porosity ϕ, pore radius r and tortuosity T. This equation predicts a linear relationship between k and ϕ and a proportionality $k \sim r^2$. The ratio T/ϕ in the CBM corresponds to the resistivity formation factor F, which can be derived from geoelectrical measurements on clean formations with known water conductivity. The resulting proportionality $k \sim 1/F$ is only valid for formations with a constant pore radius. However, most rocks exhibit a pore radius distribution. The problem is overcome by the use of an effective hydraulic radius r_{eff}. The surface conductivity sensed with geoelectrical measurements increases with increasing internal surface area and provides a proxy measure of r_{eff}. The imaginary part of conductivity recorded with induced polarization is proportional to surface conductivity and thus facilitates permeability estimation from geoelectrical measurements. However, F has proven to be the major parameter in k-prediction. Given a strong relationship between F and r_{eff} for most rock formations, a power-law relationship $k \sim F^{-\beta}$ is implicit to reliable k-prediction.

1 Introduction

Porosity (ϕ) and permeability (k) are key parameters in characterizing reservoir properties of oil and gas deposits, aquifers, and formations for potential carbon dioxide storage or the use of geothermal energy. Whereas ϕ can be easily determined from geophysical parameters acquired in boreholes or by surveys on the Earth's surface, k-prediction from geophysical measurements remains a challenge. The nuclear magnetic resonance (NMR) method is well established for the determination of permeability from well logs [1]. The NMR method provides the porosity and the relaxation time distribution that is closely related to the pore radius distribution. Porosity and pore radius are the key parameters for the determination of permeability [2]. However, we focus in our study on the potential of geoelectrical methods for k-prediction. Considering the similarity between fluid and current flow in the interconnected pore space of porous media, a variety of theoretical and empirical models have been proposed that relate electrical parameters to k [3]. However, most of these models are only valid for single rock formations.

The used models are based on the capillary bundle model (CBM) that relates k to geometrical parameters like porosity ϕ, the pore radius r and the tortuosity T. We replace the geometrical parameters by quantities that can be determined from geoelectrical measurements including methods like induced polarization (IP) that provide the complex electrical conductivity.

Using a comprehensive database composed of 282 samples originating from different sandstone, carbonate, and mudstone formations, we investigate the relationships between geometrical and geoelectrical parameters and evaluate the validity of the proposed models for k-prediction.

2 Permeability models

2.1. Capillary bundle model

The combination of the Hagen-Poiseuille Law, which describes the fluid flow through a cylindrical tube, with Darcy's Law, which relates the pressure gradient and flow rate, results in a fundamental equation [4, 5, 6]

$$k = \frac{r^2}{8} \cdot \frac{\phi}{T} \qquad (1)$$

that corresponds to the CBM. It formulates permeability as a function of quantities that characterize the geometry of the pore space. Equation 1 predicts a linear relationship between k and ϕ and a proportionality $k \sim r^2$. Assuming equal tortuosity of the hydraulic and electric path through

* Corresponding author: andreas.weller@tu-clausthal.de

the porous medium, the ratio ϕ/T can be replaced by the inverse of the resistivity formation factor F [4, 5]:

$$k = \frac{r^2}{8F}. \quad (2)$$

Equation 2 suggests a proportionality $k \propto 1/F$. On the other hand, we find $k \propto r^2$ that underlines the strong dependence of k on the pore radius. The CBM assumes a fixed value r for all capillaries.

However, most rocks exhibit a pore radius distribution. The problem can be overcome by the definition of an effective hydraulic radius [4]

$$r_{eff} = \sqrt{8kF}. \quad (3)$$

This quantity can be determined for known values of k and F.

2.2 Geoelectrical parameters

The formation factor was originally introduced as a geoelectrical parameter that represents the ratio between the conductivity of the pore-saturating fluid (σ_w) and the conductivity of the fully saturated porous rock (σ_0) assuming that the mineral framework is non-conductive [7]. However, the electrical double layer (EDL) forming between the pore filling fluid and the solid mineral grains contributes to the electrical conductivity of the rock. The EDL is characterized by an increased ion concentration relative to that of the saturating fluid. The additional contribution of the EDL to the rock conductivity is called surface conductivity (σ_{surf}). Assuming that electrolytic conductivity (σ_{el}) and surface conductivity act in parallel, the rock conductivity can be presented by [8]

$$\sigma_0 = \sigma_{el} + \sigma_{surf} = \frac{1}{F}\,\sigma_w + \sigma_{surf}\,. \quad (4)$$

Multi-salinity experiments with varying fluid conductivity σ_w are performed to determine both F and σ_{surf}. In the case of high-salinity brines ($\sigma_w \gg \sigma_{surf}$), the contribution of σ_{surf} becomes negligible and F can be approximated by the ratio σ_w/σ_0.

F is closely related to porosity [7]:

$$F = \phi^{-m}, \quad (5)$$

with m being the cementation factor. Therefore, knowing ϕ and m, F can be estimated. Access to the pore radius by electrical measurements is via the surface conductivity, which increases with rising internal surface area. The parameter S_{por} defines the ratio between the surface area A and the pore volume V_{por} of the rock sample. Assuming cylindrical capillaries, we get [4]

$$S_{por} = \frac{A}{V_{por}} = \frac{2}{r}. \quad (6)$$

Assuming that surface conductivity σ_{surf} is proportional to S_{por}/F [9], we find with equation 6

$$\sigma_{surf} \propto \frac{S_{por}}{F} = \frac{2}{rF}. \quad (7)$$

However, determining the surface conductivity is a challenging procedure requiring time-consuming multi-salinity experiments.

An alternative approach is based on the spectral induced polarization (SIP) method that records a complex electrical conductivity as a function of frequency f:

$$\sigma_0^*(f) = \frac{1}{F}\sigma_w + \sigma_{surf}^*(f) \quad (8)$$

Considering that the electrolytic conductivity of the saturating fluid contributes only to the real part of rock conductivity (σ_0'), we find for the real part of σ_0^*

$$\sigma_0'(f) = \frac{1}{F}\sigma_w + \sigma_{surf}'(f). \quad (9)$$

The imaginary part of rock conductivity (σ_0'') originates only from the surface conductivity

$$\sigma_0''(f) = \sigma_{surf}''(f). \quad (10)$$

Experimental studies have shown that σ_{surf}' and σ_{surf}'' are proportional to each other [10]. Considering this proportionality and equation 7, the pore radius can be expressed by [11, 12]:

$$r \propto \frac{1}{F\,\sigma_0''}. \quad (11)$$

Inserting this proportionality in equation 2, the permeability can be expressed by

$$k = \frac{a_q}{F^3(\sigma_0'')^2}. \quad (12)$$

The factor a_q in the numerator takes into account the relationship between the electrochemical properties of the EDL and the strength of polarization that is expressed by σ_0''. Equation 12 confirms that k-prediction can be fully related to parameters derived from geoelectrical measurements.

2.3 Porosity-permeability relationships

In practical applications, direct relationships between ϕ and k are preferred. We show why the so-called *poro-perm* relationships are only valid for single formations. A generalization should be avoided.

Considering the CBM in equation 1, and assuming a constant pore radius in the formation, we find the *poro-perm* relationship $k \propto \phi$.

However, it can be assumed that the pore radius depends on porosity for most formations. In analogy to equation 6, we consider the surface area of the pore space per unit solid (or grain) volume:

$$S_{solid} = \frac{A}{V_{solid}} = \frac{\phi}{1-\phi}\frac{A}{V_{por}} = \frac{\phi}{1-\phi}\,\frac{2}{r} = \frac{2e}{r}, \quad (13)$$

with e being the void ratio

$$e = \frac{V_{por}}{V_{solid}} = \frac{\phi}{1-\phi}, \quad (14)$$

and r represents the radius of the pore. Using equation 13, the CBM in equation 1 reads

$$k = \frac{e^2}{2S_{solid}^2}\frac{\phi}{T} = \frac{\phi^3}{(1-\phi)^2}\frac{1}{2T\,S_{solid}^2} = \frac{\phi^3}{(1-\phi)^2}\frac{c_0}{S_{solid}^2}, \quad (15)$$

which corresponds to the formulation of the Kozeny-Carman equation with a fixed shape factor $c_0 = \frac{1}{2T} = \frac{1}{5}$ [13]. Regarding spherical grains with a grain radius r_g, we get

$$S_{solid} = \frac{A}{V_{solid}} = \frac{4\pi r_g^2}{\frac{4}{3}\pi r_g^3} = \frac{3}{r_g}, \quad (16)$$

and

$$k = \frac{\phi^3}{(1-\phi)^2}\frac{r_g^2}{18\,T}. \quad (17)$$

Considering formations with a uniform grain radius and constant tortuosity, we expect a *poro-perm* relationship $k \propto \phi^3$.

Following an approach of Amaefule et al. [14], a *Reservoir Quality Index* (*RQI*) is introduced with

$$RQI = \sqrt{\frac{k}{\phi}} = \frac{r_{eff}}{\sqrt{8T}}, \quad (18)$$

that proves to be a similar quantity like the effective hydraulic radius, which is defined in equation 3. Both quantities provide a length (in meters) that is related to the pore radius. The ratio r_{eff}/RQI only depends on the square root of tortuosity.

A second parameter referred to as *Flow Zone Indicator* (*FZI*) is defined [14]:

$$FZI = \frac{RQI}{e} = \frac{1}{\sqrt{2T}S_{solid}}. \quad (19)$$

Assuming that *FZI* is a constant for each formation, the *k*-prediction in equation 1 can be simplified to

$$k = \frac{\phi^3}{(1-\phi)^2}\, FZI^2. \quad (20)$$

Comparing equations 17 and 20, we find another formulation for *FZI*:

$$FZI = \frac{r_g}{3\sqrt{2T}} \quad (21)$$

Equation 20 describes another *poro-perm* relationship $k \propto \phi^3$, because it shows only a dependence on porosity if a variation in *FZI* is ignored.

3 Samples

We compiled a large dataset acquired from petrophysical investigations on 282 rock samples originating from sandstone, mudstone, and carbonate formations. Most of these samples have already been investigated in previous studies. The sandstones include 26 samples from the Fontainebleau Formation (France) [15], 24 samples from the Sherwood Formation (UK) [16], 24 samples from the Shahejie Formation (China) [17], 43 samples from the Bahariya Formation (Egypt) [18, 19], 14 samples from the Araba Formation (Egypt) [20], 17 samples from the Nubia Formation (Egypt) [21], 16 samples from the Tushka region in Egypt [21], 11 samples from the Santa Susanna Formation (USA) [22], and 21 samples from the Hydrite Formation (USA) [22]. The carbonates include 21 samples from the USA [23] and 42 samples from the Tushka region in Egypt [24]. A set of 23 mudstones samples from USA [25] completes the database. More information about the samples can be found in the provided references.

The petrophysical measurements of all samples have been done in the laboratories of Rutgers University in Newark (USA), LIAG Institute of Applied Geophysics in Hannover (Germany), and Clausthal University of Technology (Germany). Permeability, porosity and formations factor are available for all samples. Additionally, SIP measurements have been performed over a wide frequency range (mostly between 0.1 and 1000 Hz). The imaginary part of conductivity σ_0'' measured at a reference frequency of f = 1 Hz and a water conductivity of 0.1 S/m is used as a proxy for the strength of polarization.

Considering the complete dataset, the permeability covers a wide interval from $3 \cdot 10^{-20}$ m² to $8 \cdot 10^{-12}$ m². A wide variation in k is a prerequisite for a reliable test of *k*-prediction models. The porosity ranges from 0.96 % to 34.7 %. The formation factor varies between 4.3 and 9880. The imaginary part of conductivity σ_0'' ranges between 0.8 and 1000 µS/m.

4 Results

4.1. General relationships

Considering the CBM, the most relevant parameters for *k*-prediction are porosity, tortuosity and pore radius. Fig. 1 displays the relationship between measured permeability and porosity. Although a general increase of k for rising ϕ is observed, the figure confirms that there exists no general *poro-perm* relationship. Looking at a porosity of ϕ = 0.1, we find a variation of k over five orders of magnitude. The coloured solid lines indicate the resulting power-law fit for each formation. We find power-law exponents in the range between close to zero for the Santa Susana and Hydrite Formations and 15 for the Araba Formation. The highest reliability of the power-law fits are indicated for the Fontainebleau samples with an exponent of 5.62 and a coefficient of determination R^2 = 0.861.

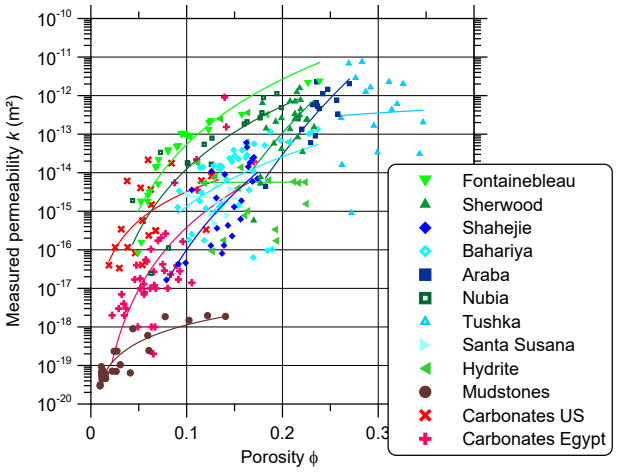

Fig. 1. Relationship between porosity and permeability for all samples. The coloured solid lines indicate the resulting power-law fit for each formation.

The expected decrease of k with rising T can be observed for most formations in Fig. 2. The solid lines indicate the result of a power-law fit with exponents varying between -10.3 for the Araba Formation and -2.0 for the mudstones.

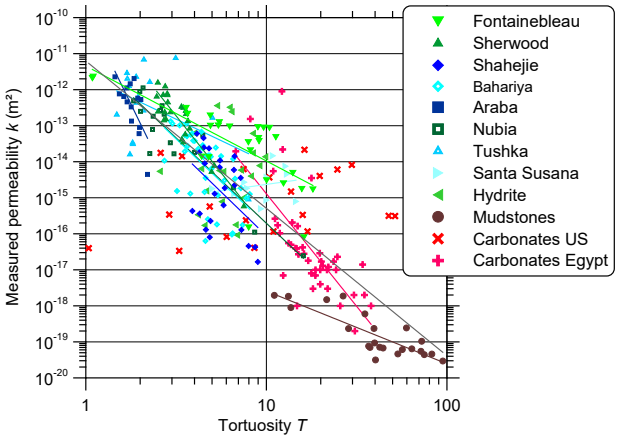

Fig. 2. Relationship between tortuosity and permeability for all samples. The coloured solid lines indicate the resulting power-law fit for each formation.

Equation 2 suggests a decrease of k with rising formation factor that can be observed in Fig. 3. The exponents β of the power-law fit $k \sim F^{-\beta}$ vary between 1 for the mudstones and 5 for the Sherwood formation.

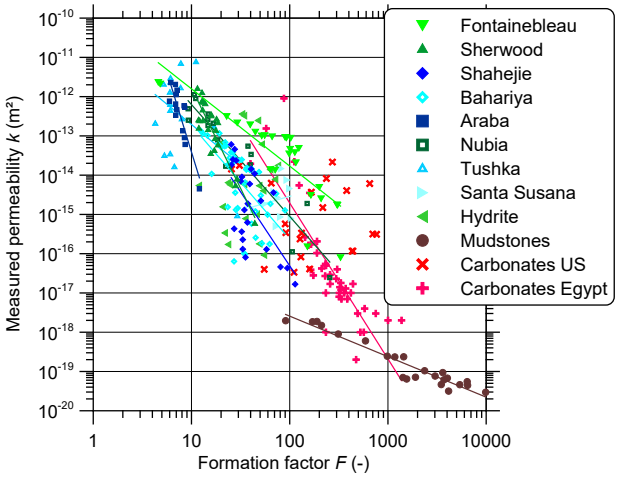

Fig. 3. Relationship between formation factor and permeability for all samples. The coloured solid lines indicate the resulting power-law fit for each formation.

Regarding the CBM in equations 1 and 2, the pore radius has a strong effect on k. The effective hydraulic radius that has been determined using equation 3 replaces the pore radius in equations 1 and 2. Fig. 4 indicates a reliable fit of the relationship between r_{eff} and measured permeability. The resulting exponents of a power-law fit vary in a narrow range between 1.72 for the Santa Susana Formation and 2.79 for the Fontainebleau Formation. Most of the exponents are close to two as predicted by the CBM.

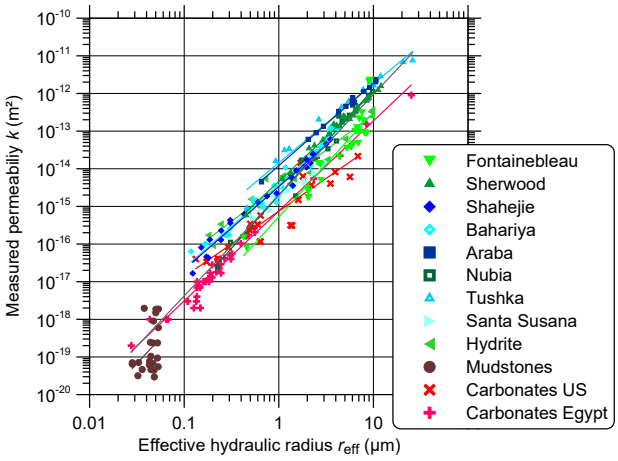

Fig. 4. Relationship between effective hydraulic radius and permeability for all samples. The coloured solid lines indicate the resulting power-law fit for each formation.

Fig. 5 shows the relationship between σ_0'' and measured permeability. Considering equation 12, a decreasing k is expected with increasing imaginary part of conductivity. However, we do not observe a uniform trend. Some formations show an increasing k with rising σ_0'', e.g. Nubia, mudstone formations and the Egyptian carbonates, whereas other formations show a reverse trend, e.g. Araba Formation and the carbonates from the USA. For other formations, the observed trend are not reliable considering the low values of the coefficient of determination ($R^2 < 0.2$), e.g. for Fontainebleau, Sherwood, Shahejie, and Bahariya Formations.

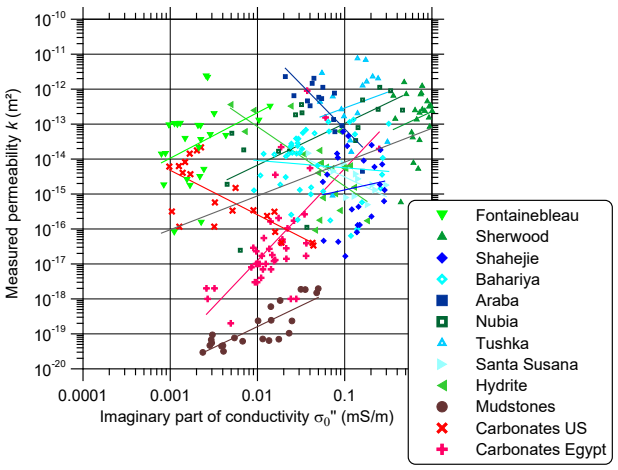

Fig. 5. Relationship between imaginary part of conductivity and permeability for all samples. The coloured solid lines indicate the resulting power-law fit for each formation.

4.2. Relationships of *RQI* and *FZI*

We investigated the potential of *RQI* and *FZI* for permeability prediction in our study. Fig. 6 displays the relationship between *RQI* and permeability. In comparison with Fig. 4, we find less scatter in the resulting graphs. The exponents of the fitting power-laws vary between 1.97 and 2.37 for the considered formations.

Only the mudstone formation provides a higher exponent with 3.34. Ignoring the mudstone samples, we get a power-law fit:

$$k = 1.75\ 10^{-13}\ (RQI)^{2.22}, \qquad (22)$$

with a coefficient of determination $R^2 = 0.986$. Therefore, the *RQI* seems to have a huge potential in *k*-prediction. However, equation 22 cannot be used for *k*-prediction because the measured permeability is required to determine *RQI* for each sample. *RQI* varies with both porosity and permeability and is not a quantity that characterizes a formation, but a single sample.

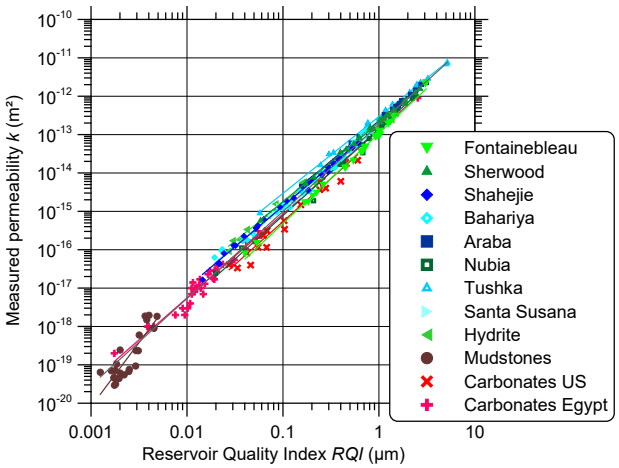

Fig. 6. Relationship between Reservoir Quality Index and permeability for all samples. The coloured solid lines indicate the resulting power-law fit for each formation.

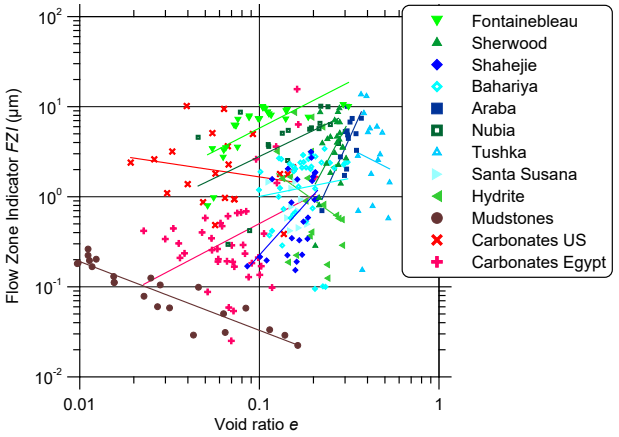

Fig. 7. Relationship between Flow Zone Indicator and void ratio for all samples. The coloured solid lines indicate the resulting power-law fit for each formation.

However, *RQI* is closely related to *FZI* as indicated by equation 19. The approach of Amaefule et al. [14] assumes that samples with constant *FZI* represent similar pore throat attributes and thereby constitute a *hydraulic unit*. Fig. 7 displays the relationship between *FZI* and *e*. We find a wide variation of *FZI* for most formations. Therefore, the samples of a single formation do not represent the same *hydraulic unit*. The power-law fit of the relationships $FZI \sim e$ represent different trends. For most formations, we observe an increase of *FZI* with rising *e* (e.g. Fontainebleau, Araba, and Nubia Formations), whereas a decrease is observed for the mudstone samples.

4.3. Permeability prediction

Following the explanations in chapter 2, equation 12 is recommended for *k*-prediction on the basis of geoelectrical parameters. Using a uniform factor $a_q = 0.8$ nS², Fig. 8 compares the predicted *k* with the measured *k*. The general trend is properly reflected by the data of most formations. However, we find a considerable overestimation of *k* for the samples of the Fontainebleau Formation. On the other hand, equation 12 underestimates *k* for the Sherwood Formation. It can be concluded that the choice of a uniform value for a_q does not consider the varying relationship between the electrochemical properties of the EDL and the imaginary part of conductivity.

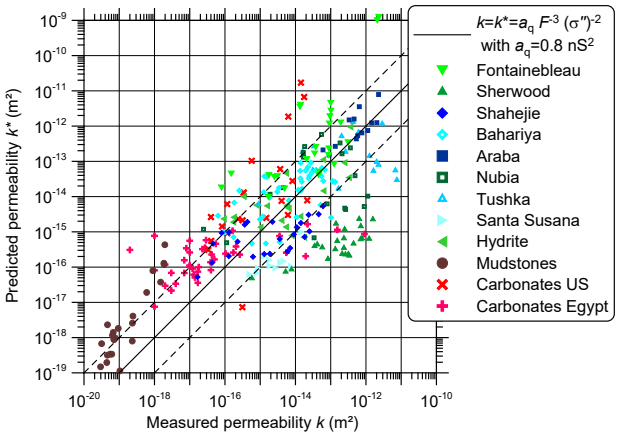

Fig. 8. Comparison of measured and predicted permeability for all samples with a uniform factor a_q. The two dashed lines indicate a deviation of one order of magnitude from the measured permeability.

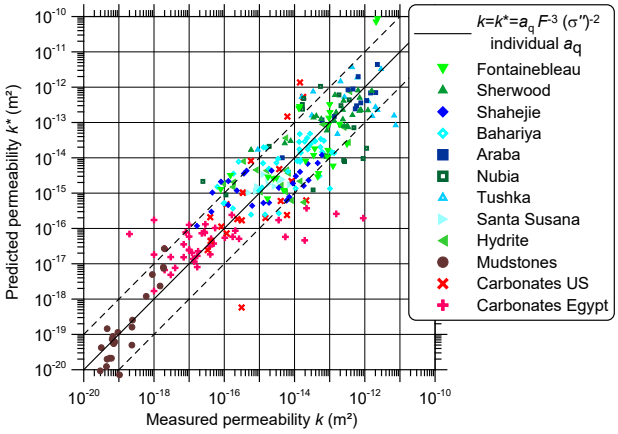

Fig. 9. Comparison of measured and predicted permeability for all samples with individual factors a_q for each formation. The two dashed lines indicate a deviation of one order of magnitude from the measured permeability.

We determined an individual value of a_q for each formation by equalizing the geometric mean values of predicted and measured permeability values. Using these individual factors a_q, which are compiled in Table 1, the agreement between measured and predicted permeability is improved as shown in Fig. 9.

Table 1. Factors a_q of equation 12 determined for the different formations.

Formation	a_q in S²
Fontainebleau	$5.41 \cdot 10^{-20}$
Sherwood	$2.78 \cdot 10^{-16}$
Shahejie	$1.79 \cdot 10^{-18}$
Bahariya	$4.21 \cdot 10^{-19}$
Araba	$4.47 \cdot 10^{-19}$
Nubia	$1.45 \cdot 10^{-18}$
Tushka	$2.25 \cdot 10^{-18}$
Santa Susana	$1.32 \cdot 10^{-17}$
Hydrite	$6.33 \cdot 10^{-19}$
Mudstones	$4.99 \cdot 10^{-20}$
Carbonates US	$6.38 \cdot 10^{-20}$
Carbonates Egypt	$1.80 \cdot 10^{-19}$
All	$\mathbf{8.00 \cdot 10^{-19}}$

We determined the geometric mean of *FZI* from the samples of each formation. With these mean values, we determined k using the *poro-perm* equation 20. Fig. 10 compares the predicted k with the measured k. Considering the whole dataset, the general trend is well reproduced by the *poro-perm* prediction. However, we find that the variability in measured k is not properly reflected by the predicted k for samples of formations with a low range in porosity (e.g. Sherwood, Shahejie, Araba, and Hydrite Formations).

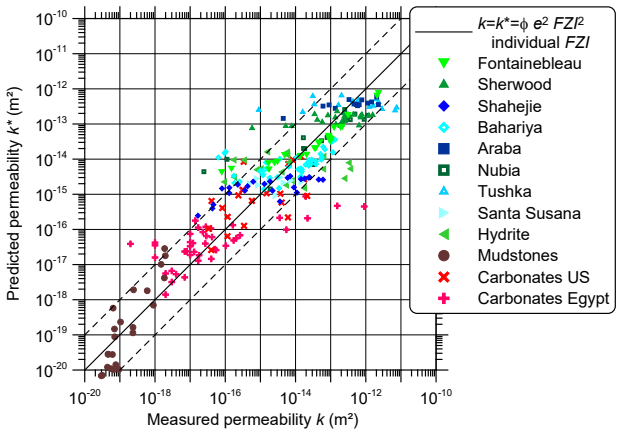

Fig. 10. Comparison of measured and predicted permeability for all samples with individual factors *FZI* for each formation. The two dashed lines indicate a deviation of one order of magnitude from the measured permeability.

5 Discussion

5.1. Evaluation of *poro-perm* relationships

A close relationship between ϕ and k is only observed if the other geometric parameters in the CBM-formulation of equation 1 remain more or less unchanged or show a close relation to ϕ. Looking at Fig. 1, we find reliable *poro-perm* relationships only for the mudstones with

$$k^* = 3.49 \cdot 10^{-17} m^2 \, \phi^{1.49} \; (R^2 = 0.819) \qquad (23)$$

and the Fontainebleau sandstones with

$$k^* = 2.28 \cdot 10^{-8} \, m^2 \phi^{5.62} \; (R^2 = 0.861). \qquad (24)$$

The non-integer exponents of ϕ result from equation 1 under the consideration of the relationships between (a) r_{eff} and ϕ, and (b) between T and ϕ.

For the mudstones, mercury intrusion porosimetry indicated nearly the same pore radius for all samples [25]. Assuming a constant pore radius ($r \propto \phi^0$), and a proportionality $T \propto \phi^{-0.45}$, we predict the exponent of ϕ with $0 + 1 - (-0.45) = 1.45$. The resulting exponent of 1.45 is close to the ϕ-exponent in equation 23.

For the samples of Fontainebleau Formation, we find $r_{eff} \propto \phi^{1.56}$ and $T \propto \phi^{1.42}$. Regarding equation 1, we predict the exponent of ϕ with $2 * (1.56) + 1 - (-1.42) = 5.54$. Again, the resulting exponent is close to the ϕ-exponent in equation 24.

Fig. 11 shows the relationships determined between the parameters of the CBM (equation 1 in blue). For the Nubia, Sherwood, and Araba Formations, a similar calculation shows a good agreement between predicted and calculated ϕ-exponents.

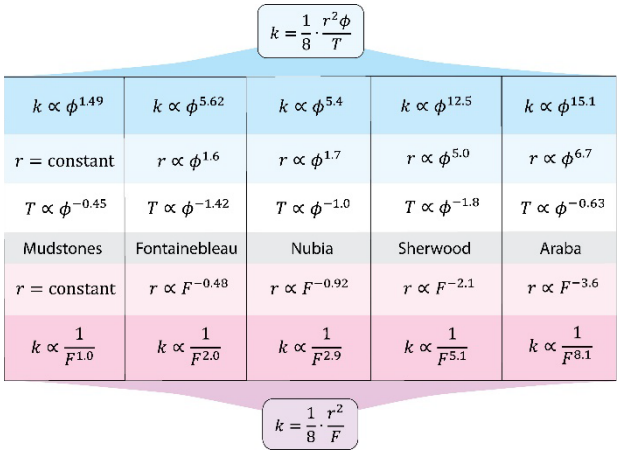

Fig. 11. Relationships between the parameters of the Capillary Bundle Model of equation 1 (in blue) and equation 2 (in pink) for selected formations.

Another type of *poro-perm* relationship is based on the concept of *FZI*. As shown in equation 20, a formation with a constant value of FZI results in a *poro-perm* relationship with $k \propto \phi^3$. Unfortunately, we did not identify any formation in our study that is characterized by a constant *FZI*.

5.2. Evaluation *F-k* relationships

A close relationship between F and k is observed if the pore radius in the CBM-formulation of equation 2 remains more or less unchanged or shows a close relation to F. Looking at Fig. 3, we identify for six formations a good power-law fit between F and k with different F-exponents and coefficients of determination $R^2 > 0.68$. We present again the fit of the mudstone samples with

$$k^* = 2.97 \cdot 10^{-16} m^2 F^{-1.03} \ (R^2 = 0.924) \quad (25)$$

and the Fontainebleau sandstones with

$$k^* = 1.47 \cdot 10^{-10} m^2 F^{-1.97} \ (R^2 = 0.716). \quad (26)$$

The exponents of F result from equation 2 under the consideration of a relationship between r and F.

For the mudstone samples, we found a constant pore radius ($r \propto \phi^0$). Regarding equation 2, an F-exponent of -1 can be expected that is close to the exponent in equation 25.

For the samples of Fontainebleau Formation, we find $r_{eff} \propto F^{-0.48}$. Regarding equation 2, we predict the exponent of F with $2 * (-0.48) - 1 = -1.96$. Again, the resulting exponent is close to the F-exponent in equation 26.

Fig. 11 shows the relationships determined between the parameters of the CBM (equation 2 in pink). For the Nubia, Sherwood, and Araba Formations, a similar calculation shows a good agreement between predicted and calculated F-exponents.

We find that the CBM properly explains the determined exponents for both ϕ and F.

Six formations out of 12 enable a k-prediction based only on the geoelectrical parameter F with an equation of the type:

$$k^* = a_F F^{-\beta}. \quad (27)$$

However, the exponent β and the prefactor a_F vary from one formation to another. They have to be calibrated by laboratory investigations.

5.3. Evaluation of permeability prediction by two geoelectrical parameters

Considering the CBM with equation 2, it seems to be necessary to integrate two independent parameters in the k-prediction. The first parameter should be F that replaces the ratio T/ϕ. We have demonstrated that the effective pore radius can be replaced by a proportionality to $\frac{1}{F\sigma_0''}$. Equation 12 represents the resulting k-prediction model.

The comparison of the results of k-prediction based on this equation shows that the use of an individual factor a_q is required to get an acceptable predictive quality for most formations. However, a larger number of samples indicate a deviation of more than one order of magnitude from the measured k. Most outliers belong to the carbonate samples, whereas the sandstones and mudstones show less deviation. It should be considered that the Egyptian carbonate samples are classified into three microfacies [24]. It remains questionable whether the use of a uniform factor a_q for all microfacies is justified.

The CBM, which is the theoretical basis for the k-prediction in equation 12, assumes a capillary pore network. The presence of fractures in rocks may alter the flow regime and cause deviations in the measured permeability.

6 Conclusions

The CBM provides a reliable theoretical basis for models of k-prediction. The original form suggests an independence of porosity, tortuosity, and pore radius. However, the parameters of most investigated formations show strong interrelationships between the geometric quantities.

For most formations, simple *poro-perm* relationships are not able to provide an acceptable k-prediction. Regarding the CBM, *poro-perm* relationships are only valid either for formations with a uniform pore radius (e.g. mudstones) or strong correlations between the geometric quantities (e.g. Fontainebleau Formation).

We evaluated the potential of *RQI* and *FZI* for k-prediction. A closer look at the definition shows that the *RQI* is closely related to r_{eff}. Although the two quantities indicate a strong correlation to k, they cannot be used for k-prediction, because k has to be known to get the sample-specific values of these parameters.

For formations with a constant *FZI*, the *poro-perm* relationship $k \propto \phi^3$ can be formulated. However, none of the investigated formations shows a constant value of *FZI*.

The replacement of the ratio T/ϕ by the formation factor reveals a close relationship between k and F that can be formulated by a power-law as indicated in equation 27. However, we find a wide variation in the resulting power-law exponent β. The relationship between structural and textural properties of the formations and the value of β will be investigated in a forthcoming study.

We get access to the pore radius via the surface conductivity sensed with geoelectrical measurements, which increases with rising internal surface area. For a capillary tube, the specific surface area per unit pore volume S_{por} and r are inversely related. The imaginary part of conductivity resulting from measurements of induced polarization can be used as a proxy for the surface conductivity. The incorporation of σ_0'' into models of k-prediction fulfils its expectation only if a formation-specific factor a_q is used that reflects the relationship between EDL properties and polarization strength. The determination of the appropriate factor a_q requires expensive core analyses including measurements of spectral induced polarization.

Our study provides a laboratory-based validation of theoretical models that enable k-prediction from both geoelectrical field surveys and electrical well logging. The formation factor and the imaginary conductivity are the key parameters that have to be determined with appropriate measurements. First successful applications of k-prediction based on IP field data have already been

published [26]. IP measurements integrated in near-surface drilling technique (Ellog auger drilling [27]) provide logging-while drilling IP data that can be used for *k*-prediction [28]. Ore exploration is the traditional application of IP logging tools for the mining industry. However, IP logging can also be successfully used for applications related to geothermal projects [29]. The models for *k*-prediction presented in our study indicate the promising potential of geoelectrical methods for surface geophysical and logging applications.

We thank H. Abuseda, A. M. El-Sayed, D. Flath, M. Halisch, J. Robinson, and Z. Zhang for providing access to their data sets.

References

1. G. R. Coates, L. Xiao, M. G. Prammer, *NMR logging principles and applications* (Halliburton Energy Services, Houston)
2. A. Weller, Z. Zhang, Geophysics, **87**, M179-M188 (2022)
3. L. Slater, Surveys in Geophysics, **28**, 169-197 (2007)
4. H. Pape, L. Riepe, J. R. Schopper, The Log Analyst, **23**, 5-13 (1982)
5. M.S. Paterson, Mechanics of Materials, **2**, 345-352 (1983)
6. J. B. Walsch, W. F. Brace, JGR, **89**, 9425-9431 (1984)
7. G. E. Archie, Trans AIME, **146**, 54-63 (1942)
8. M. Rink, J. R. Schopper, *Proceedings SPWLA 15th Annual Symposium*, paper J (1974)
9. A. Weller, L. Slater, Geophysics, **77**, D185-D198 (2012)
10. F. D. Börner, *Proceedings of the Third European Core Analysis Symposium*, 359-386 (1992)
11. Q. Niu, M. Prasad, A. Revil, M. Saidian, Geophysics, **81**, E297-E309 (2016)
12. A. Weller, L. Slater, Near Surface Geophysics, **17**, 581-594 (2019)
13. J. Bear, *Dynamics of fluids in porous media* (Dover Publications, 1988)
14. J. O. Amaefule, M. Altunbay, D. Tiab, D. G. Kersey, D. K. Keelan, SPE 26436 (1993)
15. M. Halisch, S. Kruschwitz, A. Weller, B. Mensching, L. Gürlich, SCA2017-035 (2017)
16. D. Flath, *The low-frequency complex electrical response of brine-saturated shaly sandstones* (University of Birmingham, 1989)
17. Z. Zhang, A. Weller, Geophysics, **79**, D377-D387 (2014)
18. M. Halisch, A. Weller, C.-D. Sattler, W. Debschütz, A. M. El-Sayed, Petrophysics, **50**, 478-497 (2009)
19. H. Abuseda, A. Weller, C.-D. Sattler, W. Debschütz, Arab J Geosci, **9**, 212 (2016)
20. M. Kassab, A. Weller, H. Abuseda, Arab J Geosci, **15**, 944 (2022)
21. M. Kassab, A. Weller, Journal of Petroleum Science and Engineering, **78**, 310-315 (2011)
22. J. Robinson, L. Slater, A. Weller, K. Keating, T. Robinson, C. Rose, B. Parker, WRR, **54** (2018)
23. K. Peshtani, L. Slater, Geophys. J. Int., **240**, 279-289 (2025)
24. M. A. Kassab, A. Weller, Egyptian Journal of Petroleum, **28**, 189-196 (2019)
25. K. Peshtani, A. Weller, L. Slater, WRR, **60** (2024)
26. P. K. Maurya, N. Balbarini, I. Møller, V. Rønde, A. V. Christiansen, P. L. Bjerg, E. Auken, G. Fiandaca, Geophys. J. Int., **213**, 770-785 (2018)
27. K.I. Sørensen, F. Larson, Ground Water Monitoring & Remediation, 19, 97-101 (1999)
28. G. Fiandaca, P. K. Maurya, N. Balbarini, A. Hördt, A. V. Christiansen, N. Foged, P. L. Bjerg, E. Auken, WRR, **54** (2018)
29. L. Lévy, D. A. Ciraula, B. Legros, T. Martin, A. Weller, JGR: Solid Earth, **129** (2024).